

Utilizing an electron redistribution strategy to inhibit the leaching of sulfur from CeO₂/NiCo₂S₄ heterostructure for high-efficiency oxygen evolution

Peng Wang, Xiao Han, Ping Bai, Jiarong Mu, Yihua Zhao, Jinlu He ^{*}, Yiguo Su ^{*}

Inner Mongolia Key Laboratory of Chemistry and Physics of Rare Earth Materials, School of Chemistry and Chemical Engineering, Inner Mongolia University, Hohhot 010021, People's Republic of China



ARTICLE INFO

Keywords:

Chalcogenides
Heterogeneous interface
Oxygen evolution reaction
Stable
High current density

ABSTRACT

Developing highly active and robust transition metal chalcogenides (TMCs) electrocatalysts toward oxygen evolution reaction (OER) remains a challenge. Herein, we report an electron redistribution mechanism that involves the metal-sulfur (M-S) bond stabilization triggered by electron transfer from Ce to Ni and Co in CeO₂/NiCo₂S₄ heterostructure, thereby effectively inhibiting the leaching of sulfur from CeO₂/NiCo₂S₄ during the OER process. Moreover, the well-modulated heterogeneous interface enables optimal adsorption affinity for oxygen intermediates and reduces the energy barrier of OER. As a result, CeO₂/NiCo₂S₄ exhibits superior OER activity with ultralow overpotentials of 146 and 271 mV at 10 and 100 mA cm⁻², respectively. More importantly, CeO₂/NiCo₂S₄ possesses excellent durability for over 200 h at 500 mA cm⁻², surpassing individual NiCo₂S₄ and most of the reported TMCs-based electrocatalysts. This work provides new insights for achieving good compatibility of TMCs-based OER electrocatalysts in terms of high activity and stability.

1. Introduction

Electrochemical water splitting serves as a promising technology for the mass production of renewable hydrogen energy [1]. Unfortunately, its extensive implementation is significantly restricted by the anodic OER characterized by sluggish four-proton-coupled electron transfer steps [2,3]. Currently, noble metal oxides such as RuO₂ and IrO₂ have emerged as the most successful commercially viable electrocatalysts for the OER. However, their exorbitant costs and limited durability under high current densities pose significant obstacles to their widespread implementation [4]. Therefore, the development of low-cost, stable, and highly efficient non-precious-metal electrocatalysts is crucial. TMCs, with adjustable electronic structure and controllable morphology, have been extensively investigated for their potential in catalyzing the OER [5–7]. However, the catalytic performance of TMCs still falls short compared to that of noble metal-based electrocatalysts due to their insufficient active sites, inadequate stability, and poor hydrophilicity [8].

The previous studies have demonstrated that the highly oxidative nature of the OER process inevitably triggers the reconstruction of TMCs. This irreversible transformation typically leads to undesired modifications in both structure and composition, thereby diminishing

catalyst lifetime and disrupting the delicate balance between activity and stability [9,10]. The significant dissolution of the S element is primarily attributed to the facile disruption of chemical bonds between sulfur and low-value metals under higher OER overpotentials, resulting in a complete transformation of TMCs into oxyhydroxides with diminished conductivity. As a result, this process weakens the charge-transfer kinetics for the OER [11]. Additionally, such a complete transformation process is typically accompanied by catalyst loss due to weakened adhesion between the catalyst and the substrate, as well as catalyst agglomeration, resulting in a significant reduction in the number of accessible active sites and consequently diminishing catalytic performance [12]. Moreover, the reaction interface, which consists of solid, liquid, and gas phases, exhibits a highly intricate nature. Therefore, it is imperative to enhance the hydrophilicity and bubble release behavior of the TMCs in order to augment their mass transport capacity for efficient and stable operation during the OER process [13]. The aforementioned issues continue to pose significant challenges in achieving highly efficient and stable operation of TMCs under industrial conditions [14,15].

Interfacial engineering serves as an effective strategy to further enhance the catalytic efficiency and modify the physical and chemical characteristics of electrocatalysts, encompassing reactant accessibility and surface wettability [16]. The construction of heterogeneous

* Corresponding authors.

E-mail addresses: hejinlu@imu.edu.cn (J. He), cesyg@imu.edu.cn (Y. Su).

interfaces is prevailing approach among them, wherein variations in energy band structures, disparities in majority carrier concentrations, and Fermi energy levels result in alterations in chemical composition and charge distribution. Consequently, remarkable synergistic effects are observed, enabling heterostructures to surpass individual materials [17,18]. For example, Zhang and co-workers reported NiFe₂O₄/FeNi₂S₄ heterostructures containing abundant interfaces. The findings indicated that these oxide/sulfide interfaces effectively regulate the binding energy between catalysts and oxygen intermediates, thereby promoting the kinetics of the OER [19]. Shen and co-workers coupled Co₉S₈ with N, S codoped carbon matrix (Co₉S₈@NS-C) to modulate the interface properties [20]. The synergistic effects between NS-C layers and Co₉S₈ effectively regulated the Fermi levels of each other, resulting in Co₉S₈@NS-C exhibiting enhanced adsorption energy for oxygen intermediates compared to individual Co₉S₈ and NS-C. However, in these studies, the stability of their TMCs-based electrocatalysts was only able to sustain continuous operation for a limited duration of several dozen hours at a relatively low current density (e.g. 10 mA cm⁻²), which falls short of meeting the requirements for industrial applications. Besides, identifying active sites remains a challenge because of the intricate structure and electronic processes at the interface. Due to the low covalency of M-S bonds resulting from the significant electronegativity difference between S and transition metals, selecting a suitable co-catalyst to balance the electron density of metal and S is an effective approach for enhancing the covalency of M-S bonds. Given the advantageous ionic properties exhibited by the rare earth (RE)-O bond [21], it is hypothesized that the formation of the RE-oxide/sulfide heterostructure offers a potential avenue for realizing the conservation of the M-S bond covalency by effectively extracting electrons from adjacent RE atoms. The exceptional characteristics of CeO₂, such as its high stability, remarkable hydrophilicity, and excellent affinity for oxygen-containing species, make it a frequently employed material for interface design [22, 23]. The previous studies have indicated that the flexible transition between Ce³⁺ and Ce⁴⁺ could offer a multitude of mobile electron transfer stations for various reactions due to the unique valence electron configuration of Ce element ($4f^1 5d^1 6s^2$) [24].

Herein, NiCo₂S₄ nanoparticles were uniformly anchored on CeO₂ nanorods with a high surface area to construct RE-oxide/sulfide heterostructures (CeO₂/NiCo₂S₄) for efficient OER. The optimized CeO₂/NiCo₂S₄ outperforms individual NiCo₂S₄ and the commercial IrO₂ with lower overpotentials (146 and 271 mV at 10 and 100 mA cm⁻²) and higher stability. The X-ray photoelectron spectroscopy (XPS) analysis reveals that the introduction of CeO₂ facilitates electron donation from Ce to Ni and Co, thereby achieving electron density balance among Ni, Co, and S. The XPS and energy dispersive X-ray spectroscopy (EDS) results after the stability test reveal a suppressed extraction of S from NiCo₂S₄ during the OER process, which can be attributed to the enhanced covalency of (Ni, Co)-S bonds upon the introduction of CeO₂. The density functional theory (DFT) results further validate that the electronic donation from Ce atoms strengthens the covalency of (Ni, Co)-S bonds by regulating the electron density of Ni, Co, and S. As a result, it enhances the formation energy of S vacancies (S_V) and hinders the reconstruction of NiCo₂S₄. Additionally, the electronic structure of CeO₂/NiCo₂S₄ is effectively modulated by harnessing the synergistic effects between CeO₂ and NiCo₂S₄, thereby facilitating charge transfer and providing a suitable adsorption strength for oxygen intermediates to enhance the activity of the OER.

2. Experimental section

2.1. Sample preparation

2.1.1. Pretreatment of carbon cloth (CC)

A piece of CC measuring 2 × 1 cm was submerged in a solution of nitric acid, with a volume of 30 mL. The system was then placed inside an autoclave lined with Teflon and heated to a temperature of 140 °C for

a duration of 5 h. Subsequently, the CC underwent an ultrasonic treatment lasting for 20 min in three separate solutions - acetone, ethanol, and ultrapure water. Finally, it was dried under vacuum conditions at a temperature of 60 °C.

2.1.2. Synthesis of CeO₂ nanorods

The solution was prepared by dissolving 0.612 g of hexadecyl trimethyl ammonium bromide (CTAB) and 0.552 g of citric acid in a mixture consisting of 35 mL ethylene glycol and 35 mL ultrapure water. Subsequently, the above solution was supplemented with 0.327 g of Ce (NO₃)₃·6 H₂O, which was slowly added while continuously stirring at 25 °C for 1 h until complete dissolution occurred. The resulting mixture was then transferred to a Teflon-lined stainless-steel autoclave and maintained at 180 °C for 8 h. Following this step, the precipitate underwent repeated washing using ethanol and ultrapure water before being dried at a temperature of 60 °C to yield Ce(OH)₃ powder as the final product. Lastly, the obtained Ce(OH)₃ powder underwent further processing in a muffle furnace operating at 550 °C for 5 h to obtain CeO₂ nanorods.

2.1.3. Synthesis of the CeO₂/NiCo₂S₄ catalyst

A clean CC was placed in a 20 mL of mixed solution containing Co (NO₃)₂·6 H₂O (1.5 mmol, 0.44 g), Ni(NO₃)₂·9 H₂O (1.5 mmol, 0.44 g), CH₄N₂O (15 mmol, 0.9 g), and pre-prepared CeO₂ (1.5 mmol, 0.26 g). The aforementioned solution was transferred into a Teflon-lined autoclave and maintained at 120 °C for 12 h. Subsequently, the CeO₂/NiCo layered double hydroxide (CeO₂/NiCo-LDH) product was obtained after cooling to room temperature, followed by three rounds of washing with ultrapure water and ethanol, and finally dried at 60 °C. The precursor CeO₂/NiCo-LDH underwent in-situ transformation into CeO₂/NiCo₂O₄ after annealing at 450 °C. Subsequently, a solution was prepared by dissolving 2.7 mmol of thioacetamide in 20 mL of ultrapure water, and a piece of CeO₂/NiCo₂O₄ was immersed in the solution. Afterwards, the system was transferred into a Teflon-lined autoclave and maintained at 160 °C for 10 h. Subsequently, the CeO₂/NiCo₂S₄ catalyst was formed, followed by thorough rinsing with ultrapure water and ethanol, and finally dried at 60 °C. For comparison, NiCo₂S₄ was prepared using the same strategies but without using CeO₂. In addition, to explore the effects of different CeO₂ content on catalytic performance, a series of CeO₂/NiCo₂S₄ catalysts were obtained by adjusting the initial mass of CeO₂ in the composite (0.75, 1.5, 2.25, and 3 mmol).

2.2. Material characterization and electrochemical measurements and computational details

The material characterization, electrochemical measurements, and computational details are detailed in [supporting information](#).

3. Results and discussion

3.1. Theoretical perspective on the inhibitory effect of electron redistribution strategy on S leaching

Due to the significantly higher electronegativity of S element compared to transition metal, the charge distribution in TMCs predominantly localizes around the S atom, resulting in weakened covalent bonding between transition metal and S. Considering the intrinsic higher energy level of f orbitals and the facile valence electronic donation for RE species [21], when constructing RE-oxide/sulfide heterostructure, it is expected that RE species will induce interfacial electron redistribution to balance the electron density between the transition metal and S. This ultimately strengthens the covalency of the Metal-S bond.

The rational construction of RE-oxide/sulfide heterostructure model catalysts is critical for the accomplishment of the theoretical hypothesis above. The high stability, excellent hydrophilicity, and flexible

switching between Ce^{3+} and Ce^{4+} make CeO_2 as a frequently utilized material in interface design among RE materials [24]. Moreover, NiCo_2S_4 is selected as the OER active species due to its the high electrical conductivity, multiple valences, and surface reconstruction characteristic at oxidation potentials [5]. The construction of $\text{CeO}_2/\text{NiCo}_2\text{S}_4$ as a model catalyst holds great promise for analyzing the feasibility of the electron redistribution strategy in inhibiting the leaching of S element in TMCs.

The regulations of interfacial electronic structure modulation for $\text{CeO}_2/\text{NiCo}_2\text{S}_4$ heterostructure are theoretically profiled by DFT. The optimized structural models of $\text{CeO}_2/\text{NiCo}_2\text{S}_4$, CeO_2 , and NiCo_2S_4 are illustrated in Fig. 1a. According to the charge differential density test results (Fig. S1a), a significant charge redistribution is observed at the

heterogeneous interface of $\text{CeO}_2/\text{NiCo}_2\text{S}_4$, with electrons being transferred from CeO_2 to NiCo_2S_4 . Furthermore, based on the Bader charge analysis (Fig. S1b), it can be observed that in comparison with CeO_2 and NiCo_2S_4 , there is an increase in charge density for both Ni (from 75.43 to 76.67) and Co (from 131.69 to 135.59), whereas a decrease is observed for Ce (from 194.16 to 193.86). These findings provide evidence for the electron-accepting behavior exhibited by Ni and Co, along with the electron-donating characteristic displayed by Ce, thus further indicating electron migration from Ce towards Co and Ni. After the introduction of CeO_2 , the charge density of Ni, Co, and S in $\text{CeO}_2/\text{NiCo}_2\text{S}_4$ is effectively regulated. This redistribution of surface charge density indicates that electron density conservation can be shared among the Co, Ni, and S sites in (Ni, Co)-S bonds when electrons are transferred from Ce to Ni

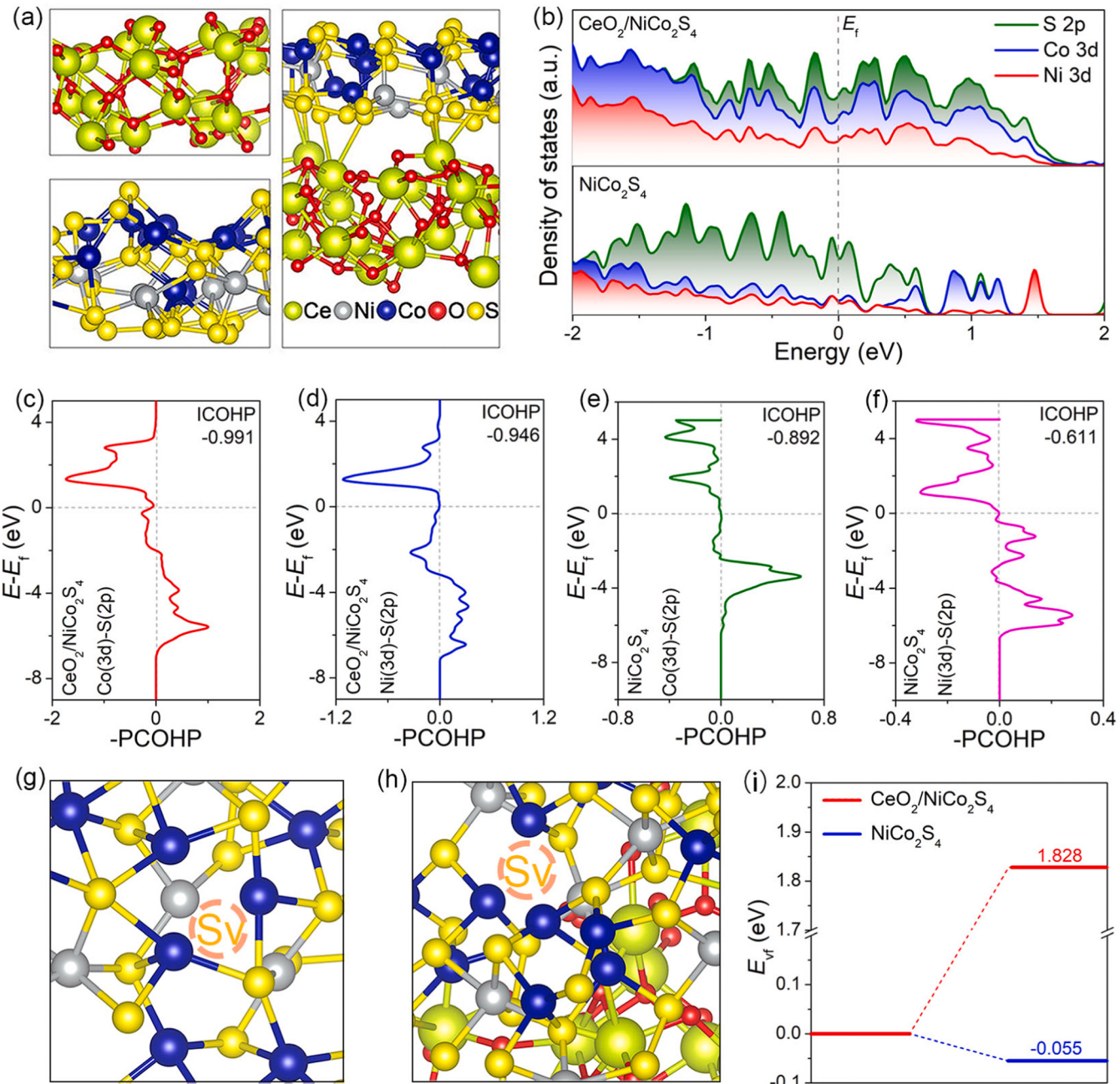


Fig. 1. (a) The theoretical models of the optimized configurations of CeO_2 , NiCo_2S_4 , and $\text{CeO}_2/\text{NiCo}_2\text{S}_4$. (b) The PDOS for the Ni 3d, Co 3d, and S 2p of $\text{CeO}_2/\text{NiCo}_2\text{S}_4$ and NiCo_2S_4 . (c-f) The projected COHP for the Co-S and Ni-S interactions in $\text{CeO}_2/\text{NiCo}_2\text{S}_4$ and NiCo_2S_4 . The bonding and antibonding states are shown on the right and the left of the vertical zero line, respectively. The horizontal line indicates the Fermi level. (g, h) The structures of NiCo_2S_4 and $\text{CeO}_2/\text{NiCo}_2\text{S}_4$ with S_V. (i) The S_V formation energy of $\text{CeO}_2/\text{NiCo}_2\text{S}_4$ and NiCo_2S_4 .

and Co. This contributed to strengthening the covalency of (Ni, Co)-S bonds. Moreover, the density of states (DOS) depicted in Fig. 1b reveals a higher overlap between the binding states of Ni 3d, Co 3d and S 2p orbitals in CeO₂/NiCo₂S₄ compared to NiCo₂S₄, indicating enhanced binding of (Ni, Co) and S atoms in CeO₂/NiCo₂S₄ and the great contribution of CeO₂ to the enhancement of (Ni, Co)-S bonds covalency. Furthermore, the (Ni, Co)-S bonds strength of CeO₂/NiCo₂S₄ and NiCo₂S₄ was investigated using crystal orbital Hamilton populations (COHP). According to the ICOHP theory, positive and negative values of ICOHP indicate bonding and antibonding interactions, respectively, while zero values correspond to nonbonding interactions [25]. The more negative the ICOHP value, the stronger the (Ni, Co)-S bonds. Therefore, the larger ICOHP value for the (Ni, Co)-S bonds in CeO₂/NiCo₂S₄, as depicted in Fig. 1c-f, provides evidence for the enhanced stability of these bonds compared to individual NiCo₂S₄.

Additionally, the complexity of removing a sulfur atom bonded to Ni and Co in CeO₂/NiCo₂S₄ and NiCo₂S₄ systems was investigated by calculating the formation energy (E_{vf}) of S_v, aiming to further validate the feasibility of incorporating CeO₂ for enhancing the stability of NiCo₂S₄. Fig. 1g-i demonstrate that the inclusion of CeO₂ significantly enhances the E_{vf} value of CeO₂/NiCo₂S₄ compared to NiCo₂S₄ alone, indicating a suppression in sulfur removal/dissolution from NiCo₂S₄ due to the introduction of CeO₂. The aforementioned theoretical calculations demonstrate that the covalency and strength of M-S bonds can be effectively enhanced through an electron redistribution strategy induced by CeO₂, thereby inhibiting the leaching of S elements from NiCo₂S₄. These results provide important theoretical support for us to design a stable CeO₂/NiCo₂S₄ electrocatalyst reasonably.

3.2. Synthesis and structural characteristics of CeO₂/NiCo₂S₄

The growth process of the CeO₂/NiCo₂S₄ heterostructure on CC is illustrated in Fig. 2a. Firstly, CeO₂ nanorods were synthesized through a facile hydrothermal and calcination process. Subsequently, a clean CC was submerged in a mixed solution comprising Ni(NO₃)₂·6H₂O, Co (NO₃)₂·6H₂O, and pre-prepared CeO₂. The aforementioned mixed solution underwent hydrothermal treatment to obtain CeO₂/NiCo-LDH hybrids. The precursor CeO₂/NiCo-LDH underwent in-situ transformation into CeO₂/NiCo₂O₄ after annealing at 450 °C. Finally, the CeO₂/NiCo₂S₄ was obtained through a hydrothermal pathway in the presence of thioacetamide.

The XRD patterns (Fig. 2b, S2) of the CeO₂/NiCo₂S₄ catalyst exhibits prominent diffraction peaks at 31.5°, 38.2°, 50.3°, and 55.1°, which can be attributed to the crystal planes (311), (400), (511), and (440) of the cubic NiCo₂S₄ phase, respectively (JCPDS 43-1477) [26]. Additionally, the peaks observed at 28.5°, 33.1°, 47.5°, and 56.3° correspond to the crystal planes (111), (200), (220), and (311) of the cubic CeO₂ structure, respectively (JCPDS 65-2975) [27]. Notably, no characteristic peaks associated with cerium sulfides are detected.

The scanning electron microscopy (SEM) images (Figs. S3a-d) of CeO₂/NiCo₂S₄ show that dense CeO₂/NiCo₂S₄ catalysts with rough surfaces are distributed on the CC substrate with numerous void spaces. The detailed morphological features (Figs. S4a) of CeO₂/NiCo₂S₄ were further investigated using transmission electron microscopy (TEM). NiCo₂S₄ nanoparticles with an average diameter of 17 ± 4 nm are uniformly embedded on the surface of CeO₂ nanorods to enhance the surface roughness of CeO₂ nanorods (Fig. S4b). This enhanced surface roughness can establish a readily accessible pathway for efficient mass transfer, thereby promoting the diffusion of reaction intermediates and facilitating the elimination of gas bubbles [28]. The NiCo₂S₄ nanoparticles are tightly embedded into the surface of CeO₂ nanorods, forming a heterogeneous interface, as evidenced by the enlarged TEM images (Fig. 2c). As shown in high-resolution TEM (Fig. 2d), the lattice fringes revealed in the two adjacent regions highlighted by the yellow line correspond well to the (111) plane of CeO₂ and the (311) plane of NiCo₂S₄, with interplanar distances measuring 0.312 nm and 0.284 nm,

respectively, validating the successful construction of the CeO₂/NiCo₂S₄ heterogeneous interface [29]. The findings can be additionally validated through the utilization of fast Fourier transformation (FFT) patterns (Fig. 2e). The high-angle annular dark-field scanning transmission electron microscopy (HAADF-STEM) and corresponding elemental mapping (Fig. 2f-k) reveal a uniform distribution of Ce, Ni, Co, S, and O elements throughout the CeO₂/NiCo₂S₄ heterostructure.

To study the near-surface composition and the electronic structure of catalysts, XPS was carried out. The fitted results of Ce 3d, Ni 2p, Co 2p, O 1s, and S 2p for CeO₂/NiCo₂S₄, NiCo₂S₄ and CeO₂ were all summarized in Table S1-5. The XPS survey spectrum of CeO₂/NiCo₂S₄ (Fig. 3a) confirms the coexistence of Ce, Ni, Co, S, and O. Compared to NiCo₂S₄, the peaks of Ni 2p and Co 2p peaks in CeO₂/NiCo₂S₄ shift towards a lower energy direction, and the corresponding ratios of Ni³⁺/(Ni²⁺+Ni³⁺) and Co³⁺/(Co²⁺+Co³⁺) decrease significantly (Fig. 3b, c), indicating an increase in electron density around the Ni and Co species after the formation of the heterostructure [30-32]. However, the Ce 3d peaks of CeO₂/NiCo₂S₄ exhibit positive shifts and a decrease in the Ce³⁺/Ce⁴⁺ ratio compared to CeO₂ (Fig. 3d), indicating a reduction in electron density for Ce [33,34]. This is further confirmed by the reduced peak area of oxygen vacancy in O 1s spectra and weakened EPR signal of CeO₂/NiCo₂S₄ compared to CeO₂ (Fig. S5). The above results indicate the introduction of CeO₂ induces charge redistribution at the CeO₂/NiCo₂S₄ interface, thereby facilitating electron migration from Ce to Ni and Co. Moreover, the binding energy of S 2p for CeO₂/NiCo₂S₄ exhibits a positive shift compared to NiCo₂S₄ (Fig. 3e), indicating a decrease in electron density for S. The diametrically opposite changes in electron density of Ni, Co, and S after the formation of the CeO₂/NiCo₂S₄ heterostructure further suggest that the introduced CeO₂ can reinforce the covalency of the (Ni, Co)-S bonds by regulating the electron density of Ni, Co and S, thereby restraining their breakage during the OER process. The XPS analysis results are consistent with the predictions from DFT theoretical simulations.

The surface wettability and release behavior of oxygen bubbles were investigated using contact angle (CAs) measurements for CeO₂/NiCo₂S₄ and NiCo₂S₄. Fig. 3f-i demonstrate that CeO₂/NiCo₂S₄ exhibits smaller water CAs and larger bubble CAs compared to NiCo₂S₄, indicating that the introduction of CeO₂ can enhance mass transfer and promote the release of gas bubbles at the surface of CeO₂/NiCo₂S₄. This enhancement is essential for CeO₂/NiCo₂S₄ to achieve fast reaction kinetics and excellent stability during the OER process [35].

3.3. Electrode performance and stability analyses

The OER performance of the as-prepared catalysts was measured by a standard three-electrode system in 1 M KOH solution with 90 % iR correction. The linear sweep voltammetry (LSV) curves in Fig. 4a display that CeO₂/NiCo₂S₄ exhibits significantly lower overpotentials of 146 and 271 mV to achieve current densities of 10 and 100 mA cm⁻², respectively, compared to NiCo₂S₄ (204 and 346 mV), IrO₂ (316 and 406 mV), and other control samples (Fig. S6). However, the catalytic activity for the OER is negligible in CeO₂ and CC. The CeO₂/NiCo₂S₄ catalyst, as shown in Fig. 4b, exhibits a smaller Tafel slope of 30.3 mV dec⁻¹ compared to NiCo₂S₄, CeO₂, IrO₂, and CC, suggesting that the presence of CeO₂ significantly enhanced the OER kinetics for CeO₂/NiCo₂S₄. The combined results from LSV curves and Tafel slopes provide compelling evidence for the crucial role played by CeO₂ in improving the OER performance.

To investigate the impact of introduced CeO₂ on the intrinsic OER catalytic activity of CeO₂/NiCo₂S₄, the electrochemically active surface areas (ECSAs) for NiCo₂S₄ and CeO₂/NiCo₂S₄ were determined by calculating the double-layer charge capacitance (C_{dl}) measured in the non-faradaic potential region (Figs. S7a-c). The ECSAs of CeO₂/NiCo₂S₄, as illustrated in Fig. 4c, exhibit a significantly greater magnitude compared to NiCo₂S₄, indicating that the introduction of CeO₂ can lead to enhanced ECSAs and an increase in accessible active sites. Moreover,

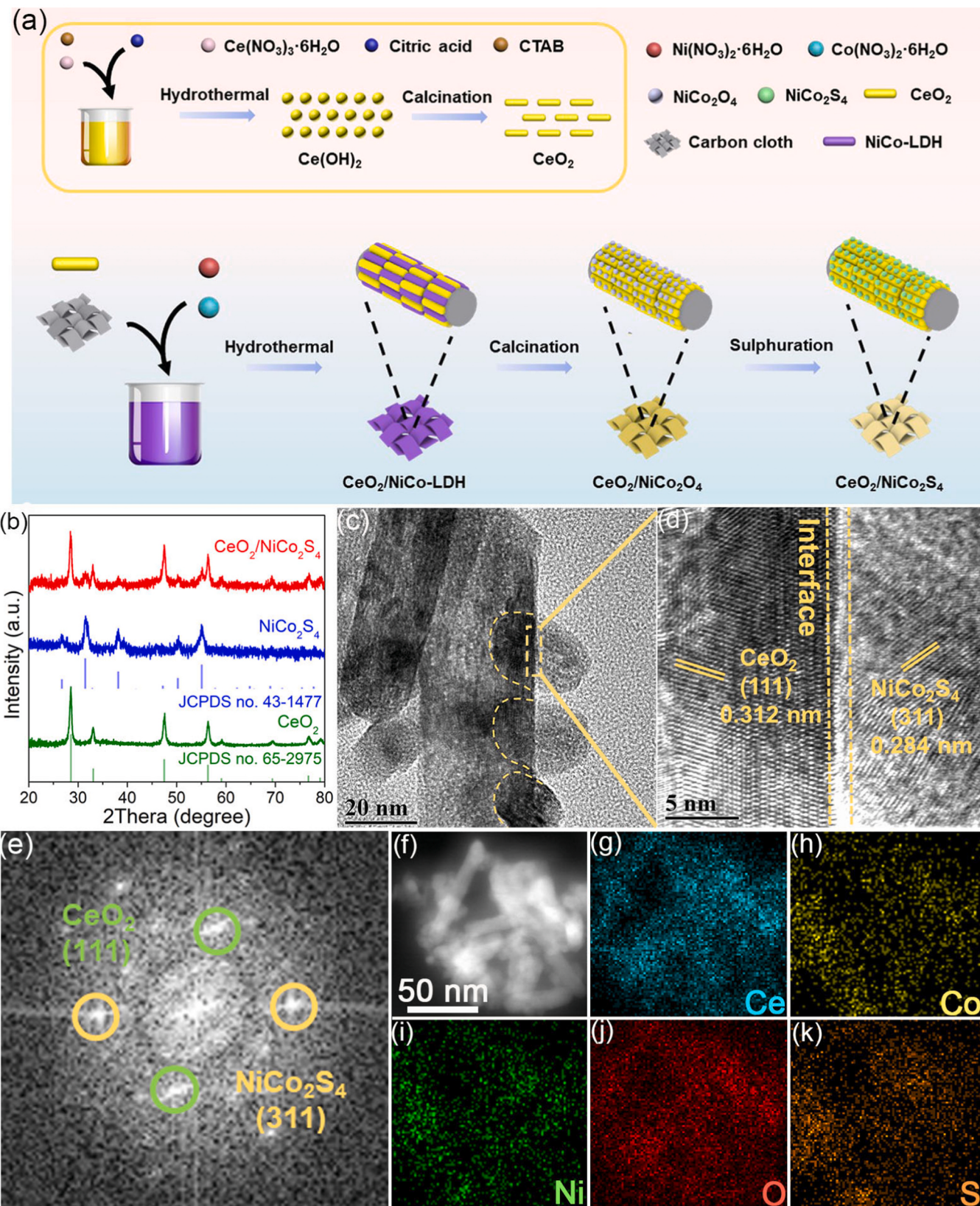


Fig. 2. (a) Synthetic scheme. (b) XRD, (c) TEM, (d) HRTEM, (e) the corresponding fast Fourier transformation mode, (f) HAADF-STEM, (g-k) elemental mapping images of $\text{CeO}_2/\text{NiCo}_2\text{S}_4$.

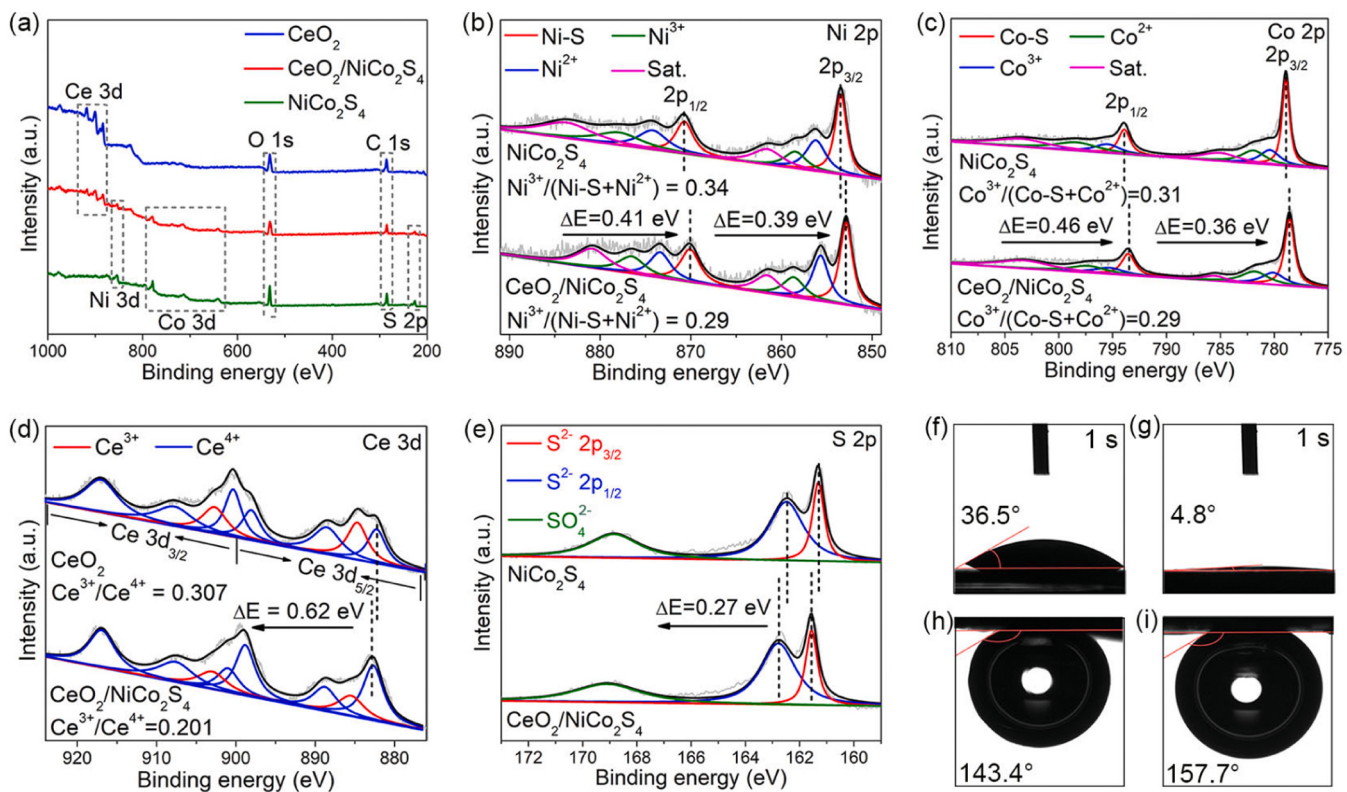


Fig. 3. (a) XPS survey spectra. XPS spectra of (b) Ni 2p, (c) Co 2p, (d) Ce 3d, (e) S 2p of as-prepared catalysts. Surface wettability and bubble releasing behavior. The photos of the surface wettability: (f) NiCo₂S₄, (g) CeO₂/NiCo₂S₄. The photos of the bubble/catalyst contact angles: (h) NiCo₂S₄, (i) CeO₂/NiCo₂S₄.

the ECSA-normalized specific activity (j_{ECSA}) was obtained and is shown in Fig. 4c and S7d. CeO₂/NiCo₂S₄ exhibits a higher intrinsic activity with $j_{\text{ECSA}} = 0.181 \text{ mA cm}^{-2}$ at 1.55 V (vs. RHE), which is approximately 1.3 times higher than that of NiCo₂S₄. This further confirms the enhanced intrinsic OER activity of CeO₂/NiCo₂S₄ compared to NiCo₂S₄ due to the introduction of CeO₂.

The charge-transfer kinetics of the as-prepared catalysts were investigated through electrochemical impedance spectroscopy (EIS). As shown in Fig. S8, CeO₂/NiCo₂S₄ exhibits a lower charge transfer resistance (R_{ct}) compared to NiCo₂S₄ alone, indicating an enhanced charge transfer kinetics in CeO₂/NiCo₂S₄. The operando EIS technique was utilized to further investigate the impact of introduced CeO₂ on the charge transfer resistance (R_{ct}) and electrocatalytic kinetics during the OER process. In the Nyquist plots of CeO₂/NiCo₂S₄ (Fig. 4d), straight lines are observed in the low potential range from 1.15 to 1.35 V (vs. RHE), indicating that charge transfer behavior is not activated due to an extremely high R_{ct} . A distinct semicircle is observed at an applied potential of 1.40 V (vs. RHE), and the corresponding Bode phase plots (inset of Fig. 4d) also exhibit an obvious arched phase angle in the low-frequency region, indicating charge transfer behavior and electrocatalytic OER occurring between 1.35 to 1.40 V (vs. RHE). However, an applied potential of up to 1.45 V (vs. RHE) is required to observe a distinct semicircle and a noticeable arched phase angle for NiCo₂S₄ (Fig. 4e and inset). Additionally, the peak phase angles in the potential range of 1.40 to 1.50 V (vs. RHE) for CeO₂/NiCo₂S₄ and NiCo₂S₄ are displayed in Fig. 4f. The lower peak phase angles observed for CeO₂/NiCo₂S₄ indicate a greater propensity for interfacial charge transfer due to the incorporation of CeO₂, thereby facilitating faster OER kinetics compared to NiCo₂S₄.

The stability of the catalyst is also a crucial indicator for assessing its suitability for industrial applications, particularly under conditions of high current density. The results of the chronopotentiometric durability test demonstrates an long-term galvanostatic stability of CeO₂/NiCo₂S₄,

as indicated by a nearly parallel $V-t$ curve maintained over 200 h at a constant current density of 500 mA cm^{-2} (Fig. 4g). However, the potential of NiCo₂S₄ without CeO₂ support shows a significant increase after approximately 20 h under identical testing conditions. The robust stability of CeO₂/NiCo₂S₄ is further demonstrated by the almost overlapped LSV curves observed after 5000 cyclic voltammetry (CV) cycles (inset of Fig. 4g), whereas a significant degradation can be seen in the LSV curve of NiCo₂S₄. Meanwhile, the EIS measurements (Fig. S9) further reveal a significant increase in the R_{ct} of NiCo₂S₄ compared to CeO₂/NiCo₂S₄ after stability testing. This suggests that NiCo₂S₄ without CeO₂ support undergoes an uncontrolled phase transition due to structural instability during strong oxidation processes, thereby impairing its electron transport capability. The ECSAs of NiCo₂S₄ without CeO₂ support show a significant decrease, in contrast to CeO₂/NiCo₂S₄, indicating the severe occlusion of accessible active sites (Fig. S10). Finally, as displayed in Fig. 4h and Table S6, CeO₂/NiCo₂S₄ exhibits prominent advantages over previously reported catalysts for the OER in terms of overpotential ($E_{j=10, 100}$), Tafel slope, CV cycling stability, and chronopotentiometric durability test results. These findings highlight its promising potential for application in water splitting.

3.4. Identification of significant differences in stability between NiCo₂S₄ and CeO₂/NiCo₂S₄ electrodes

The stability difference between NiCo₂S₄ and CeO₂/NiCo₂S₄ catalysts was investigated by conducting SEM, TEM, and XPS analyses after a 200 h stability test. By conducting element mapping analysis to investigate the alteration in bulk composition, as displayed in Fig. 5a, b, it can be observed that Ce, Ni, Co, S, and O elements remain uniformly dispersed within the CeO₂/NiCo₂S₄ structure while the intensity of S element in the NiCo₂S₄ phase exhibits a significant decrease. The EDS results (Fig. 5c, d, and Table S7, 8) notably exhibit a decrease in the S element content for NiCo₂S₄ from 44.69 at% to 0.36 at%, with its sulfur

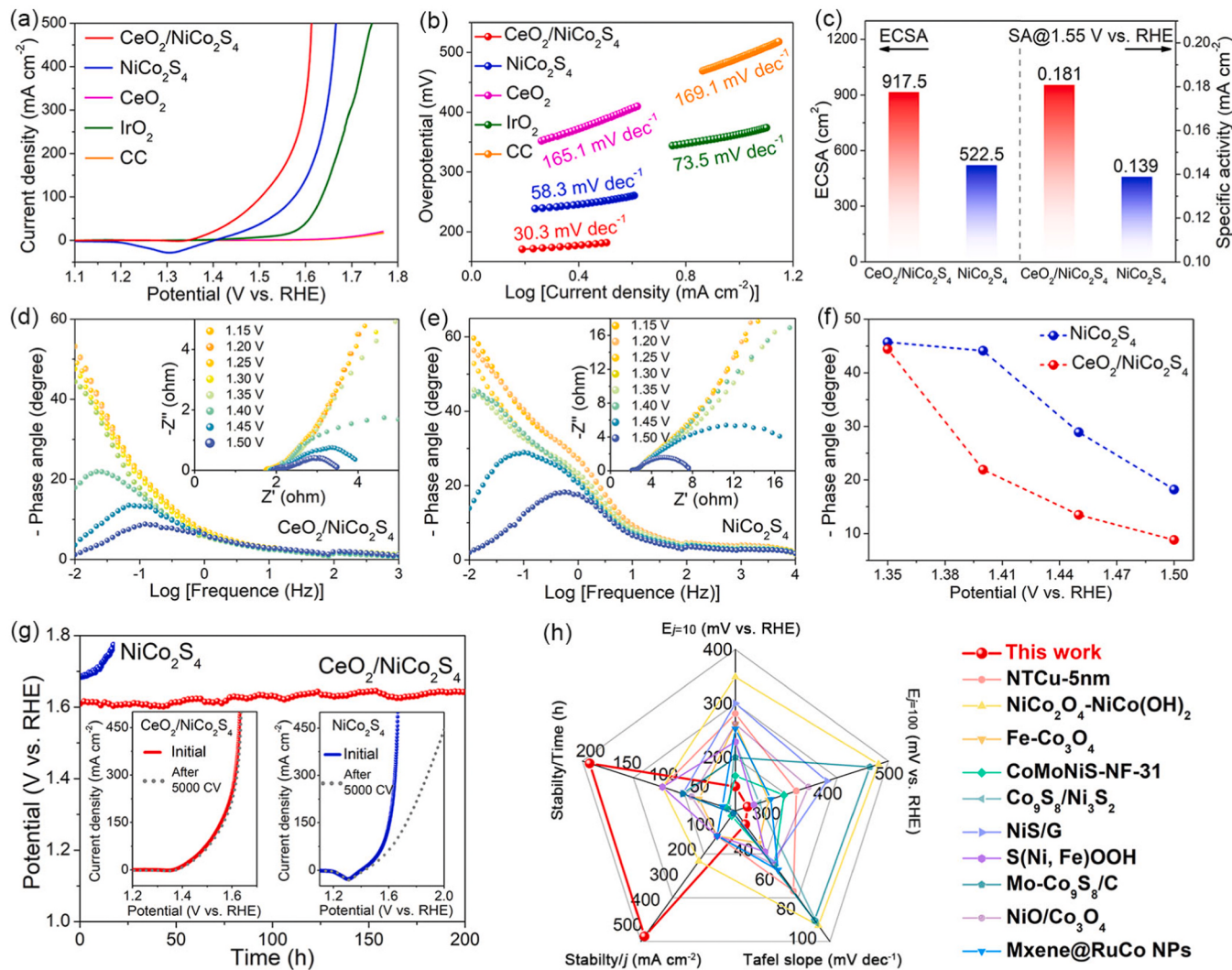


Fig. 4. (a, b) LSV curves and Tafel slopes of as-prepared catalysts. (c) ECSAs and specific activities (j_{ECSA} at 1.55 V vs RHE) of $\text{CeO}_2/\text{NiCo}_2\text{S}_4$ and NiCo_2S_4 . (d, e) Nyquist and Bode phase plots of $\text{CeO}_2/\text{NiCo}_2\text{S}_4$ and NiCo_2S_4 at different potentials (vs. RHE), respectively. (f) Phase peak angles of $\text{CeO}_2/\text{NiCo}_2\text{S}_4$ and NiCo_2S_4 at 1.35–1.50 V (vs. RHE). (g) Chronopotentiometric durability test (inset images show cycling stability tests of $\text{CeO}_2/\text{NiCo}_2\text{S}_4$ and NiCo_2S_4). (h) Comprehensive comparison of the performance of $\text{CeO}_2/\text{NiCo}_2\text{S}_4$ and other reported state-of-the-art catalysts.

loss being 3.87 times that of $\text{CeO}_2/\text{NiCo}_2\text{S}_4$. Furthermore, the XPS spectra of S 2p (Fig. 5e) after the stability test further confirm a significant decrease in sulfur content from 32.11 at% to 1.04 at%, accompanied by almost complete disappearance of the S 2p peak. These observations suggest that the M-S bonds have ruptured, which can be attributed to the complete conversion of NiCo_2S_4 into NiCo oxyhydroxides. However, the peak intensity of S 2p for $\text{CeO}_2/\text{NiCo}_2\text{S}_4$ shows a slight attenuation after the stability test, with only a decrease in the corresponding S content from 40.67 at% to 33.41 at%. The XPS analysis results indicate that the sulfur loss of NiCo_2S_4 is 5.43 times higher than that of $\text{CeO}_2/\text{NiCo}_2\text{S}_4$. The XRD patterns (Fig. 5f) obtained after the stability test reveal the absence of diffraction peaks corresponding to NiCo_2S_4 in NiCo_2S_4 without CeO_2 support, while the diffraction peaks associated with NiCo_2S_4 are well preserved in $\text{CeO}_2/\text{NiCo}_2\text{S}_4$. The entire phase reconstruction inevitably weakens the adhesion between catalysts and substrates. After the stability test, as observed in the SEM images (Fig. S11), a significant amount of NiCo_2S_4 catalysts detached from the substrate surface, while $\text{CeO}_2/\text{NiCo}_2\text{S}_4$ catalysts remained firmly attached without any noticeable detachment phenomenon. The TEM images (Fig. 5g–j) obtained after the stability test reveal a complete transformation of NiCo_2S_4 nanoparticles into low-crystallinity NiCo oxyhydroxide nanosheets in the absence of CeO_2

support. Furthermore, a significant accumulation of nanosheets is observed. However, The NiCo_2S_4 nanoparticles in $\text{CeO}_2/\text{NiCo}_2\text{S}_4$ are firmly anchored to the surface of CeO_2 , and no NiCo oxyhydroxide nanosheets are observed. Additionally, the presence of an amorphous outer layer at the periphery of NiCo_2S_4 in $\text{CeO}_2/\text{NiCo}_2\text{S}_4$ indicates selective oxidation only occurring on the edge NiCo_2S_4 to form NiCo oxyhydroxides, while a majority of the NiCo_2S_4 remains intact due to the incorporation of CeO_2 .

To further investigate the effects of electron redistribution strategy induced by CeO_2 on the leaching of S from NiCo_2S_4 , in situ Raman spectroscopy was employed to continuously monitor the surface states of both NiCo_2S_4 and $\text{CeO}_2/\text{NiCo}_2\text{S}_4$ during the OER process. In Fig. 5k, the initial NiCo_2S_4 sample exhibits characteristic Ni-S signals at 309, 361, and 386 cm^{-1} , corresponding to the stretching modes with A_1 , E , and A_1 symmetries respectively [36]. Additionally, the signals observed at 475 and 617 cm^{-1} correspond to the E_g and F_{2g} modes of the Co-S bond [37]. When the bias potential is increased to 0.2 V (vs. Hg/HgO), the Ni-S and Co-S bonds are completely eliminated, while distinct characteristic signals emerge at 478 and 1052 cm^{-1} , corresponding to Ni-O vibrations [38,39]. Additionally, signals located at 503 and 685 cm^{-1} are also observed, which pertain to the F_{2g} and A_1g modes of Co-O bond [40,41]. Notably, a distinct signal belonging to

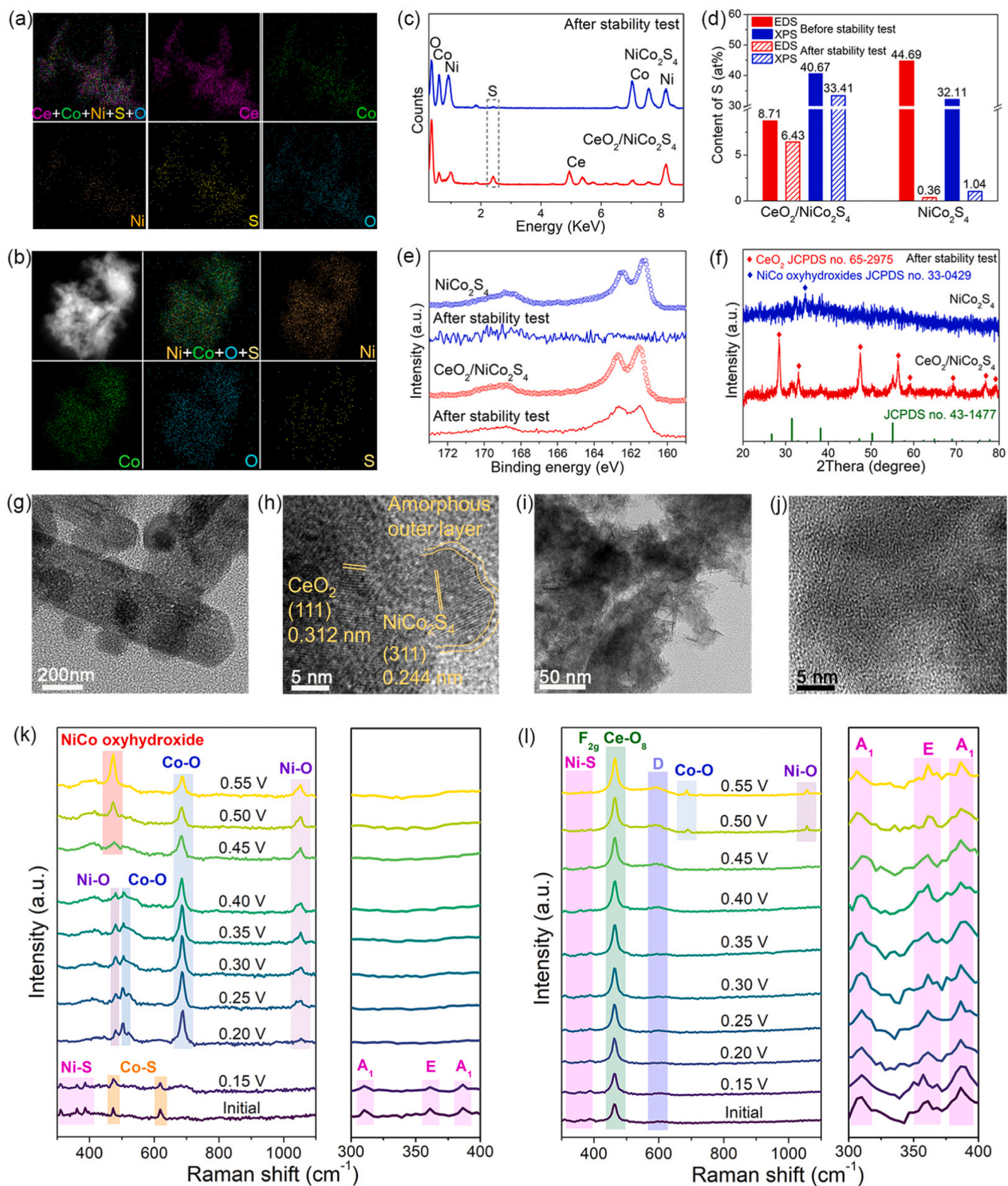


Fig. 5. (a, b) Elemental mapping images and (c) EDS spectra after stability test. (d) Quantitative analyses of CeO₂/NiCo₂S₄ and NiCo₂S₄ before and after stability testing from EDS and XPS measurements. (e) The XPS spectra of S 2p before and after stability testing. (f) XRD pattern after stability testing. TEM images of (g) CeO₂/NiCo₂S₄ and (i) NiCo₂S₄ after stability testing. HRTEM images of (h) CeO₂/NiCo₂S₄ and (j) NiCo₂S₄ after stability testing. In situ Raman spectra of (k) NiCo₂S₄ and (l) CeO₂/NiCo₂S₄.

NiCo oxyhydroxide is observed at 471 cm^{-1} after the bias potential over 0.45 V (vs. Hg/HgO). The disappearance of the Co/Ni-S bonds and the formation of the Co/Ni-O bonds with increasing voltage can be attributed to the phase transformation of NiCo_2S_4 to low-active NiCo oxyhydroxide species. As shown in Fig. 5l, the main signal present in initial $\text{CeO}_2/\text{NiCo}_2\text{S}_4$ is at 465 cm^{-1} due to the F_{2g} vibrational modes, corresponding to $\text{Ce}-\text{O}_8$ symmetric vibration [42]. Furthermore, the weak signal at 592 cm^{-1} can be ascribed to the band of defect-induced mode (D) [43]. After introducing CeO_2 , the Ni-S signals at $\text{CeO}_2/\text{NiCo}_2\text{S}_4$ surface reserved even at a high potential of 0.55 V (vs. Hg/HgO). However, due to the proximity of the signal position of Co-S to the signal position of CeO_2 , it is overwritten and thus cannot be detected. When the voltage reaches 0.50 V (vs. Hg/HgO), only weak signals of Co-O and Ni-O bonds can be observed, indicating a slight oxidation on the $\text{CeO}_2/\text{NiCo}_2\text{S}_4$ surface. In situ Raman analysis results further confirm that the presence of CeO_2 effectively prevents fracture of the metal-S bonds, thereby inhibiting leaching of S from NiCo_2S_4 during the OER process.

To explore the possibility of inhibiting the leaching of S from NiCo_2S_4 by coating. The $\text{Nb}_2\text{O}_5/\text{NiCo}_2\text{S}_4$ catalyst with a structure similar to $\text{CeO}_2/\text{NiCo}_2\text{S}_4$ was prepared using Nb_2O_5 nanorods instead of CeO_2 nanorods (Figs. S12a-d). The TEM and XPS analysis (Figs. S12e-h) of $\text{Nb}_2\text{O}_5/\text{NiCo}_2\text{S}_4$ after a 50 h stability test revealed the complete transformation of NiCo_2S_4 nanorods into NiCo oxyhydroxide nanosheets, with the characteristic peak of S 2p disappearing entirely. These findings suggest that coating alone is insufficient in preventing the leaching of sulfur from NiCo_2S_4 .

Based on the aforementioned results, we hypothesize that the inadequate stability of NiCo_2S_4 primarily stems from the excessive accumulation of nanosheets, which leads to a significant reduction in the number of accessible active sites. Furthermore, the complete transformation of NiCo_2S_4 into low-conductivity NiCo oxyhydroxides significantly hinders charge transfer kinetics for the OER. The CeO_2 nanorods effectively prevent the agglomeration of NiCo_2S_4 nanoparticles during the harsh OER process by acting as nanoislands, resulting in a uniform dispersion of NiCo_2S_4 nanoparticles on their surface in $\text{CeO}_2/\text{NiCo}_2\text{S}_4$ without any noticeable agglomeration. Furthermore, the presence of CeO_2 effectively inhibits the dissolution of S element in NiCo_2S_4 and prevents excessive reconstruction of NiCo_2S_4 , which is consistent with the predictions from DFT theoretical simulations.

3.5. Exploring the underlying reaction mechanism of intrinsic activity enhancement for $\text{CeO}_2/\text{NiCo}_2\text{S}_4$

The underlying reaction mechanisms for the enhanced intrinsic activity after uniformly anchoring NiCo_2S_4 nanoparticles on the CeO_2 support were investigated through DFT calculations. Based on the adsorption evolution mechanism (AEM), primarily involving the adsorption and desorption processes of OH^* , O^* , and OOH^* intermediates. To further validate the AEM pathway, we conducted operando differential electrochemical mass spectrometry (DEMS) experiments incorporating isotope ^{18}O -labelling measurements. As shown in Fig. S13, for the lattice oxygen mechanism (LOM)-type OER, the ^{18}O on neighboring metal sites will have probability of coupling together to form $^{36}\text{O}_2$ [29]. The signal of $^{36}\text{O}_2$ product was negligible during the OER process, while the signal of $^{32}\text{O}_2$ was observed with each CV cycle in our experiments. The DEMS results show that the occurrence of lattice oxygen evolution is insignificant during the OER process, implying the $\text{CeO}_2/\text{NiCo}_2\text{S}_4$ electrocatalyst goes through an AEM-type OER process. The DOS shown in Fig. 6a-c indicates that CeO_2 exhibits semiconductor characteristics due to its wide band gap of 1.88 eV , while the absence of a band gap for $\text{CeO}_2/\text{NiCo}_2\text{S}_4$ and NiCo_2S_4 suggests their metallic properties [5]. Besides, due to the introduction of CeO_2 , $\text{CeO}_2/\text{NiCo}_2\text{S}_4$ exhibits the highest the intensity of DOS at the Fermi energy level (E_f) compared to NiCo_2S_4 , indicating that more

electrons will be involved in the reaction, which is conductive to the acceleration of charge transfer and the enhancement of conductivity. It is noteworthy that the intensity of Co 3d orbitals around the E_f in $\text{CeO}_2/\text{NiCo}_2\text{S}_4$ exhibits a significant increase compared to both the Co 3d and Ni 3d orbitals in NiCo_2S_4 , as well as the Ni 3d orbitals in $\text{CeO}_2/\text{NiCo}_2\text{S}_4$ (Fig. 6d). This observation suggests that the DOS near E_f is primarily contributed by the Co 3d orbitals in $\text{CeO}_2/\text{NiCo}_2\text{S}_4$, indicating that Co may serve as the primary active site during the OER process.

The limiting reaction barrier and overpotential ($\eta = \max [\Delta G_1, \Delta G_2, \Delta G_3, \Delta G_4]/e - [1.23\text{ eV vs. RHE}]$) are two important descriptors for evaluating catalytic activity, which can be estimated by calculating the changes in Gibbs free energies (ΔG) of the rate-determining step (RDS) [44]. The RDS for each model and their corresponding ΔG and η values were summarized in Table S9. The four elemental steps of OER and side views of the optimized OER intermediates for the corresponding catalysts are schematically illustrated in Fig. 6e, f and S14–16. The ΔG and η values of $\text{CeO}_2/\text{NiCo}_2\text{S}_4$ (Co site) shown in Fig. 6g are comparatively lower than those of $\text{CeO}_2/\text{NiCo}_2\text{S}_4$ (Ni site), indicating that the Co site serves as the optimal active center for OER in $\text{CeO}_2/\text{NiCo}_2\text{S}_4$. Moreover, $\text{CeO}_2/\text{NiCo}_2\text{S}_4$ (Co site) exhibits the lowest ΔG and η values compared to NiCo_2S_4 (Ni site and Co site) and CeO_2 (Ce site) (Fig. 6h), which provides additional evidence that the formation of heterogeneous interfaces reduces the energy barrier for water decomposition into oxygen for $\text{CeO}_2/\text{NiCo}_2\text{S}_4$.

Interfacial electronic interactions can modulate the position of d-band center (ed) and influence the adsorption behavior of oxygen intermediates [45]. Based on the theory of ed , a higher energy level of the ed compared to the E_f results in reduced filling of antibonding states and enhanced adsorption capacity [46]. The ed values of CeO_2 (Ce site), NiCo_2S_4 (Ni site), and NiCo_2S_4 (Co site) are -3.159 , -3.748 , and -4.248 eV respectively (Fig. 6i), indicating excessive and insufficient adsorption for oxygen intermediates [47]. However, the $\text{CeO}_2/\text{NiCo}_2\text{S}_4$ (Co site) exhibits a moderate ed of -3.477 eV , which facilitates the optimization of adsorption of oxygen intermediates for enhanced catalytic activity in OER. Theoretical findings validate that electronic structure of NiCo_2S_4 can be effectively manipulated through the introduction of CeO_2 , resulting in optimized adsorption strength of oxygen intermediates and improved thermodynamic reaction energetics. This ultimately enhances the intrinsic activity for the OER.

The mechanisms of enhanced OER activity and stability for $\text{CeO}_2/\text{NiCo}_2\text{S}_4$ are summarized as schematically illustrated in Fig. 6j. In the $\text{CeO}_2/\text{NiCo}_2\text{S}_4$ heterostructure, CeO_2 can function as an electron donor to facilitate the spontaneous transfer of electrons from Ce to Co and Ni, thereby inducing charge redistribution at the heterogeneous interface. Consequently, this effectively balances the electron density surrounding the M-S bonds and enhances the covalency of the M-S bonds. Moreover, H_2O molecules are initially adsorbed onto the catalyst surface and undergo dissociation into H^* and OH^- species (Volmer step). The OH^- species are subsequently captured at the Co sites of $\text{CeO}_2/\text{NiCo}_2\text{S}_4$ heterostructure, thereby facilitating the dehydrogenation process (RDS: OH^*-O^*) by reducing the free energy in $\text{CeO}_2/\text{NiCo}_2\text{S}_4$. The OER performance of $\text{CeO}_2/\text{NiCo}_2\text{S}_4$ is excellent, as expected. The inferior activity of CeO_2 and NiCo_2S_4 can be attributed to the adsorption strength of unsuitable oxygen intermediates and the higher energy barrier for OH^* dehydrogenation caused by the suboptimal charge distribution.

4. Conclusion

In summary, we have successfully developed a unique oxide/sulfide ($\text{CeO}_2/\text{NiCo}_2\text{S}_4$) heterostructure with abundant heterogeneous interfaces. $\text{CeO}_2/\text{NiCo}_2\text{S}_4$ exhibits excellent catalytic activity, requiring overpotentials of only 146 and 271 mV to deliver current densities of 10 and 100 mA cm^{-2} , respectively. This performance surpasses that of most reported electrocatalysts based on TMCs. The experiments and DFT results confirm that the incorporation of CeO_2 effectively restricts further extraction of S from NiCo_2S_4 nanoparticles by enhancing the covalency

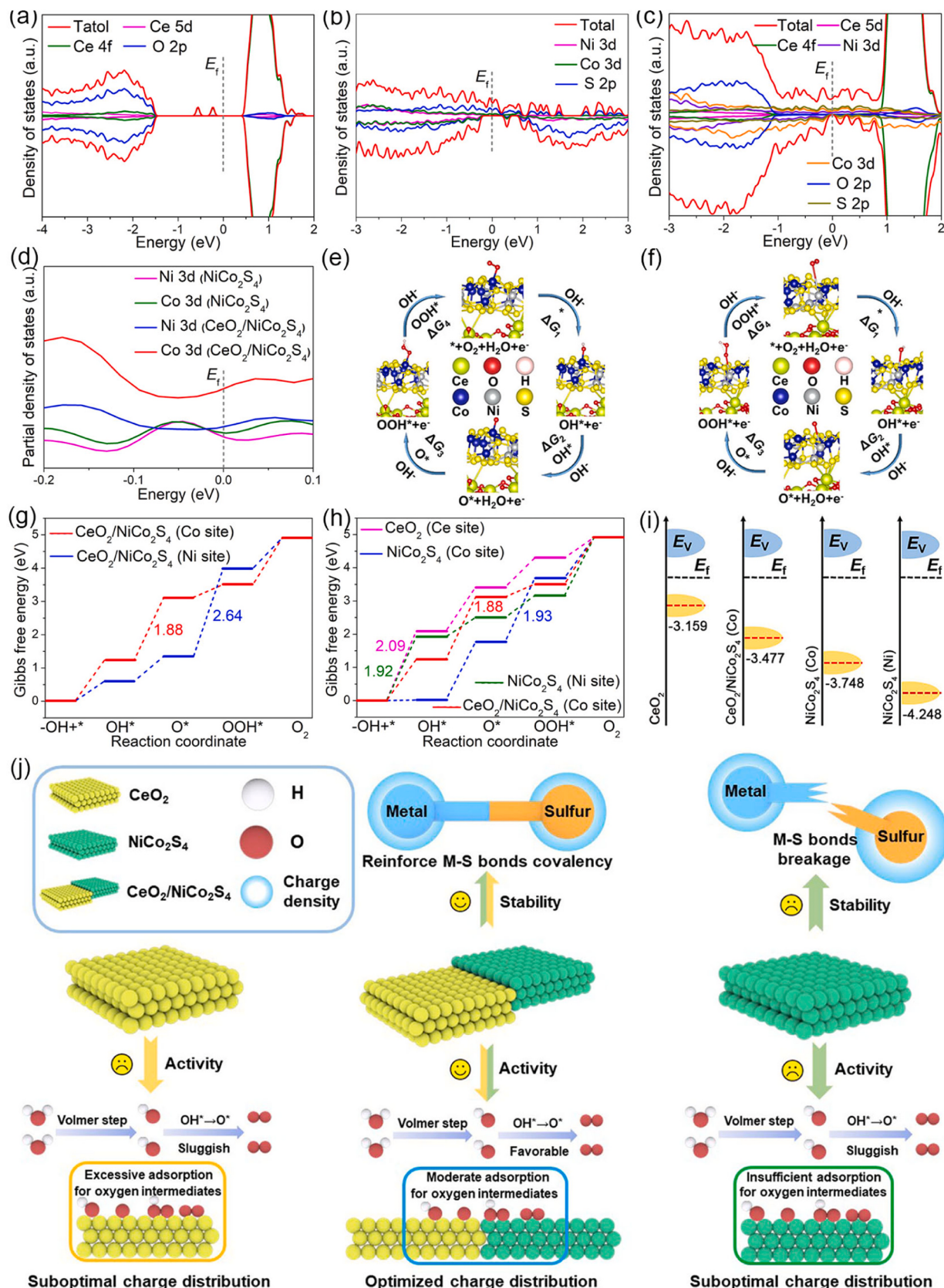


Fig. 6. (a–c) The DOS for CeO₂, NiCo₂S₄, and CeO₂/NiCo₂S₄. (d) The enlarged PDOS for the Ni 3d and Co 3d of CeO₂/NiCo₂S₄ and NiCo₂S₄. (e, f) The four elemental steps of OER and side views of the optimized OER intermediates for the Co site and Ni site of CeO₂/NiCo₂S₄. (g, h) Reaction free energy diagrams for the OER. (i) Schematic illustration of d-band center. (j) Schematic illustration of OER mechanisms for CeO₂, NiCo₂S₄, and CeO₂/NiCo₂S₄ electrocatalysts.

of (Ni, Co)-S bonds. Consequently, it significantly mitigates the reconstruction of NiCo_2S_4 , ensuring exceptional long-term stability for $\text{CeO}_2/\text{NiCo}_2\text{S}_4$ catalysts even under high current density conditions. Moreover, the $\text{CeO}_2/\text{NiCo}_2\text{S}_4$ heterogeneous interfaces in the catalysts exhibit advantageous synergistic effects, enhancing the charge transfer capability and improving the hydrophilicity and mass transport capacity of the catalysts, thereby creating an optimal and favorable interface for the OER. The present study not only offers valuable insights into the delicate balance between activity and stability of TMCs-based OER electrocatalysts, but also broadens their potential applications in various energy-related fields.

CRediT authorship contribution statement

Ping Bai: Formal analysis, Investigation. **Jiarong Mu:** Formal analysis, Investigation. **Yihua Zhao:** Investigation. **Jinlu He:** Software. **Yiguo Su:** Conceptualization, Investigation, Methodology, Resources, Supervision, Validation, Writing – review & editing. **Peng Wang:** Conceptualization, Data curation, Formal analysis, Investigation, Methodology, Writing – original draft. **Xiao Han:** Data curation, Formal analysis, Investigation.

Declaration of Competing Interest

The authors declare that they have no known competing financial interests or personal relationships that could have appeared to influence the work reported in this paper.

Data availability

Data will be made available on request.

Acknowledgements

This work was financially supported by the National Natural Science Foundation of China (Grant 22166027) and Natural Science Foundation of Inner Mongolia Autonomous Region of China (2021MS02015 and 2021MS05018).

Appendix A. Supporting information

Supplementary data associated with this article can be found in the online version at [doi:10.1016/j.apcatb.2023.123659](https://doi.org/10.1016/j.apcatb.2023.123659).

References

- [1] S.L. Zhao, C.H. Tan, C.T. He, P.F. An, F. Xie, S. Jiang, Y.F. Zhu, K.H. Wu, B. W. Zhang, H.J. Li, J. Zhang, Y. Chen, S.Q. Liu, J.C. Dong, Z.Y. Tang, Structural transformation of highly active metal-organic framework electrocatalysts during the oxygen evolution reaction, *Nat. Energy* 5 (2020) 881.
- [2] N.T. Stuen, S.F. Hung, Q. Quan, N. Zhang, Y.J. Xu, H.M. Chen, Electrocatalysis for the oxygen evolution reaction: recent development and future perspectives, *Chem. Soc. Rev.* 46 (2017) 337.
- [3] H.X. Liao, T. Luo, P.F. Tian, K.J. Chen, L.L. Lu, Y. Liu, M. Liu, J. Pan, Unveiling role of sulfate ion in nickel-iron (oxy)hydroxide with enhanced oxygen-evolving performance, *Adv. Funct. Mater.* 31 (2021) 2102772.
- [4] M.R. Liu, Q.L. Hong, Q.H. Li, Y.H. Du, H.X. Zhang, S.M. Chen, T.H. Zhou, J. Zhang, Cobalt boron imidazolate framework derived cobalt nanoparticles encapsulated in B/N codoped nanocarbon as efficient bifunctional electrocatalysts for overall water splitting, *Adv. Funct. Mater.* 28 (2018) 1801136.
- [5] J. Sun, H. Xie, N. Guo, T. Song, Y. Hao, J. Sun, J.W. Zhang, Q. Wang, Synergetic metal defect and surface chemical reconstruction into $\text{NiCo}_2\text{S}_4/\text{ZnS}$ heterojunction to achieve outstanding oxygen evolution performance, *Angew. Chem. Int. Ed.* 60 (2021) 2–9.
- [6] J. Song, C. Wei, Z.F. Huang, C. Liu, L. Zeng, X. Wang, Z.J. Xu, A review on fundamentals for designing oxygen evolution electrocatalysts, *Chem. Soc. Rev.* 49 (2020) 2196–2214.
- [7] H. Li, S. Chen, Y. Zhang, Q. Zhang, X. Jia, Q. Zhang, L. Gu, X. Sun, L. Song, X. Wang, Systematic design of superaerophobic nanotube-array electrode comprised of transition-metal sulfides for overall water splitting, *Nat. Commun.* 9 (2018) 2452.
- [8] W.H. Huang, C.Y. Su, C. Zhu, T.T. Bo, S.W. Zou, W. Zhou, Y.F. Ren, Y.N. Zhang, J. Zhang, M. Rueping, H.B. Zhang, Isolated electron trap-induced charge accumulation for efficient photocatalytic hydrogen production, *Angew. Chem. Int. Ed.* 62 (2023), e202304634.
- [9] J. Yin, J. Jin, H. Lin, Z. Yin, J. Li, M. Lu, L. Guo, P. Xi, Y. Tang, C.H. Yan, Optimized metal chalcogenides for boosting water splitting, *Adv. Sci.* 7 (2020) 1903070.
- [10] Q. Ji, Y. Kong, H. Tan, H. Duan, N. Li, B. Tang, Y. Wang, S. Feng, L. Lv, C. Wang, F. Hu, W. Zhang, L. Cai, W. Yan, Operando identification of active species and intermediates on sulfide interfaced by Fe_3O_4 for ultrastable alkaline oxygen evolution at large current density, *ACS Catal.* 12 (2022) 4318–4326.
- [11] X. Zheng, Y. Cao, Z. Wu, W. Ding, T. Xue, J. Wang, Z. Chen, X. Han, Y. Deng, W. B. Hu, Rational design and spontaneous sulfurization of NiCo-(oxy)hydroxysulfides nanosheets with modulated local electronic configuration for enhancing oxygen electrocatalysis, *Adv. Energy Mater.* 12 (2022) 2103275.
- [12] J. Masa, C. Andronescu, W. Schuhmann, Electrocatalysis as the nexus for sustainable renewable energy: the gordian knot of activity, stability, and selectivity, *Angew. Chem. Int. Ed.* 59 (2020) 15298.
- [13] P. Zhou, X.S. Lv, S.S. Liu, J.C. Wu, H.F. Wang, X.X. Wei, T.H. Wang, B. Zhou, Y. X. Lu, T. Frauenheim, X.Z. Fu, S.Y. Wang, Y.Q. Zou, Heterogeneous-interface-enhanced adsorption of organic and hydroxyl for biomass electrooxidation, *Adv. Mater.* 34 (2022) 2204089.
- [14] D.Y. Hung, P.P. Lopes, P.F.B.D. Martins, H. He, T. Kawaguchi, P. Zapol, H. You, D. Tripkovic, D. Strmcnik, Y. Zhu, S. Seifert, S. Lee, V.R. Stamenkovic, N. M. Markovic, Dynamic stability of active sites in hydr(oxy)oxides for the oxygen evolution reaction, *Nat. Energy* 5 (2020) 222.
- [15] F.Y. Chen, Z.Y. Wu, Z. Adler, H. Wang, Stability challenges of electrocatalytic oxygen evolution reaction: from mechanistic understanding to reactor design, *Joule* 5 (2021) 1704.
- [16] X.F. Zhang, W.H. Huang, L. Yu, M. García-Melchor, D.S. Wang, L.J. Zhi, H. B. Zhang, Enabling heterogeneous catalysis to achieve carbon neutrality: directional catalytic conversion of CO_2 into carboxylic acids, *Carbon Energy* (2023), e362.
- [17] J.R. Hu, Z.J. Li, D.S. Zhao, Z. Han, X.R. Wu, J.Y. Zhai, Z.Y. Liu, Y.W. Tang, G.T. Fu, L-Lysine-induced green synthesis of $\text{CoS}/\text{Co}_3\text{O}_4$ nanoframes for efficient electrocatalytic oxygen evolution, *Green. Chem.* 25 (2023) 7309–7317.
- [18] Y. Wang, X.D. Wu, X. Jiang, X.R. Wu, Y.W. Tang, D.M. Sun, G.T. Fu, Citrulline induced mesoporous CoS/CoO heterojunction nanorods triggering high-efficiency oxygen electrocatalysis in solid-state Zn-air batteries, *Chem. Eng. J.* 434 (2022), 134744.
- [19] L. An, Z. Zhang, J. Feng, F. Lv, Y. Li, R. Wang, M. Lu, R.B. Gupta, P. Xi, S. Zhang, Heterostructure-promoted oxygen electrocatalysis enables rechargeable zinc-air battery with neutral aqueous electrolyte, *J. Am. Chem. Soc.* 140 (2018) 17624–17631.
- [20] D. Lyu, S. Yao, A. Ali, Z.Q. Tian, P. Tsakaras, P.K. Shen, N. S codoped carbon matrix-encapsulated Co_9S_8 nanoparticles as a highly efficient and durable bifunctional oxygen redox electrocatalyst for rechargeable Zn-air batteries, *Adv. Energy Mater.* 11 (2021) 2101249.
- [21] M. Li, X. Wang, K. Liu, H. Sun, D. Sun, K. Huang, Y. Tang, W. Xing, H. Li, G.T. Fu, Reinforcing Co-O covalency via Ce(4f)-O(2p)-Co(3d) gradient orbital coupling for high-efficiency oxygen evolution, *Adv. Mater.* 35 (2023) 2302462.
- [22] C. Fan, X.D. Wu, M. Li, X. Wang, Y. Zhu, G.T. Fu, T.Y. Ma, Y.W. Tang, Surface chemical reconstruction of hierarchical hollow inverse-spinel manganese cobalt oxide boosting oxygen evolution reaction, *Chem. Eng. J.* 431 (2022), 133829.
- [23] X. Li, X.I.P. Hernández, Y. Chen, J. Xu, J. Zhao, C.W. Pao, C.H. Fang, J. Zeng, Y. Wang, B.C. Gates, J.Y. Liu, Functional CeO_2 nanogels for robust atomically dispersed catalysts, *Nature* 611 (2022) 284–288.
- [24] M. Li, X. Wang, K. Liu, Z.Y. Zhu, H.Y. Guo, M.Z. Li, H. Du, D.M. Sun, H. Li, K. Huang, Y.W. Tang, G.T. Fu, Ce-induced differentiated regulation of Co sites via gradient orbital coupling for bifunctional water-splitting reactions, *Adv. Energy Mater.* 13 (2023) 2301162.
- [25] X. Tan, K. Sun, Z. Zhuang, B. Hu, Y. Zhang, Q. Liu, C. He, Z. Xu, C. Chen, H. Xiao, C. Chen, Stabilizing copper by a reconstruction-resistant atomic Cu-O-Si interface for electrochemical CO_2 reduction, *J. Am. Chem. Soc.* 145 (2023) 8656–8664.
- [26] X. Shen, H. Li, Y. Zhang, T. Ma, Q. Li, Q. Jiao, Y. Zhao, H. Li, C.H. Feng, Construction dual-regulated $\text{NiCo}_2\text{S}_4@\text{Mo-doped CoFe-LDH}$ for oxygen evolution reaction at large current density, *Appl. Catal. B: Environ.* 319 (2022), 121917.
- [27] J. Liu, T. Wang, X. Liu, H. Shi, S. Li, L. Xie, Z. Cai, J. Han, Y. Huang, G. Wang, Q. Li, Reducible $\text{Co}^{3+}\text{-O}$ sites of Co-Ni-P-O_x on CeO_2 nanorods boost acidic water oxidation via interfacial charge transfer-promoted surface reconstruction, *ACS Catal.* 13 (2023) 5194–5204.
- [28] X. Shan, J. Liu, H. Mu, Y. Xiao, B. Mei, W. Liu, G. Lin, Z. Jiang, L. Wen, L. Jiang, An engineered superhydrophilic/superaerophobic electrocatalyst composed of the supported CoMoS_x chalcogel for overall water splitting, *Angew. Chem. Int. Ed.* 59 (2020) 1659–1665.
- [29] S.Y. Ge, R.K. Xie, B. Huang, Z.Y. Zhang, H. Liu, X. Kang, S.Q. Hu, S.H. Li, Y.T. Luo, Q.M. Yu, J.W. Wang, G. Chai, L.H. Guan, H.M. Cheng, B.L. Liu, A robust chromium-iridium oxide catalyst for high-current-density acidic oxygen evolution in proton exchange membrane electrolyzers, *Energy Environ. Sci.* 16 (2023) 3734–3742.
- [30] W.H. Huang, T.T. Bo, S.W. Zou, Y.Z. Wang, J.M. Chen, S. Ould-Chikh, Y. Li, W. Zhou, J. Zhang, H.B. Zhang, Surface decorated Ni sites for superior photocatalytic hydrogen production, *SusMat* 2 (2022) 466–475.
- [31] T. Wang, P. Wang, W. Zang, X. Li, D. Chen, Z. Kou, S. Mu, J. Wang, Nanoframes of $\text{Co}_3\text{O}_4\text{-Mo}_2\text{N}$ heterointerfaces enable high-performance bifunctionality toward both electrocatalytic HER and OER, *Adv. Funct. Mater.* 32 (2021) 2107382.
- [32] Y. Liu, T. Sakthivel, F. Hu, Y. Tian, D. Wu, E.H. Ang, H. Liu, S. Guo, S. Peng, Z. F. Dai, Enhancing the d/p-band center proximity with amorphous-crystalline

- interface coupling for boosted pH-robust water electrolysis, *Adv. Energy Mater.* 13 (2023) 2203797.
- [33] W.H. Huang, X.M. Li, X.F. Yang, H.Y. Zhang, P.B. Liu, Y.M. Ma, X. Lu, CeO₂-embedded mesoporous CoS/MoS₂ as highly efficient and robust oxygen evolution electrocatalyst, *Chem. Eng. J.* 420 (2021), 127595.
- [34] H. Xu, C. Shan, X. Wu, M. Sun, B. Huang, Y. Tang, C.H. Yan, Fabrication of layered double hydroxide microcapsules mediated by cerium doping in metal-organic frameworks for boosting water splitting, *Energy Environ. Sci.* 13 (2020) 2949–2956.
- [35] Q. Ji, Y. Kong, H. Tan, H. Duan, N. Li, B. Tang, Y. Wang, S. Feng, L. Lv, C. Wang, F. Hu, W. Zhang, L. Cai, W. Ya, Operando identification of active species and intermediates on sulfide interfaced by Fe₃O₄ for ultrastable alkaline oxygen evolution at large current density, *ACS Catal.* 12 (2022) 4318–4326.
- [36] S. Ghosh, B. Dasgupta, S. Kalra, M.L.P. Ashton, R.T. Yang, C.J. Kueppers, S. Gok, E. G. Alonso, J. Schmidt, K. Laun, I. Zebger, C. Walter, M. Driess, P.W. Menezes, Evolution of carbonate-intercalated γ -NiOOH from a molecularly derived nickel sulfide (pre)catalyst for efficient water and selective organic oxidation, *Small* 19 (2023) 2206679.
- [37] H. Gao, T. Zhou, Y. Zheng, Q. Zhang, Y. Liu, J. Chen, H. Liu, Z.P. Guo, CoS quantum dot nanoclusters for high-energy potassium-ion batteries, *Adv. Funct. Mater.* 27 (2017) 1702634.
- [38] H. Zhou, F. Yu, Q. Zhu, J. Sun, F. Qin, L. Yu, J. Bao, Y. Yu, S. Chen, Z.F. Ren, Water splitting by electrolysis at high current densities under 1.6 volts, *Energy Environ. Sci.* 11 (2018) 2858–2864.
- [39] J. Qin, T. Nguyen, S. Kim, Y. Lee, M. Song, W. Huang, X. Chen, T. Nguyen, I. S. Yang, Two-dimensional correlation spectroscopy analysis of Raman spectra of NiO nanoparticles, *Spectrochim. Acta A* 280 (2022), 121498.
- [40] M. Kumar, V. Bhatt, J.H. Yun, Hierarchical 3D micro flower-like Co₃O₄ structures for NO₂ detection at room temperature, *Phys. Lett. A* 384 (2020), 126477.
- [41] Q. Ji, Y. Kong, H. Tan, H. Duan, N. Li, B. Tang, Y. Wang, S. Feng, L. Lv, C. Wang, F. Hu, W. Zhao, L. Cai, W.S. Yan, Operando identification of active species and intermediates on sulfide interfaced by Fe₃O₄ for ultrastable alkaline oxygen evolution at large current density, *ACS Catal.* 12 (2022) 4318–4326.
- [42] K. Patra, Z. Liu, H. Lee, S. Hong, H. Song, H.G. Abbas, Y. Kwon, S. Ringe, J.H. Oh, Boosting electrochemical CO₂ reduction to methane via tuning oxygen vacancy concentration and surface termination on a copper/ceria catalyst, *ACS Catal.* 12 (2022) 10973–10983.
- [43] L. Yu, R. Peng, L. Chen, M. Fu, J. Wu, D.Q. Ye, Ag supported on CeO₂ with different morphologies for the catalytic oxidation of HCHO, *Chem. Eng. J.* 334 (2018) 2480–2487.
- [44] J. Sun, N.K. Guo, Z.Y. Shao, K.K. Huang, Y.W. Li, F. He, Q. Wang, A facile strategy to construct amorphous spinel-based electrocatalysts with massive oxygen vacancies using ionic liquid dopant, *Adv. Energy Mater.* 8 (2018) 1800980.
- [45] S.C. Zhang, C.H. Tan, R.P. Yan, X. Zou, F.L. Hu, Y. Mi, C. Yan, S.L. Zhao, Constructing built-in electric field in heterogeneous nanowire arrays for efficient overall water electrolysis, *Angew. Chem. Int. Ed.* 62 (2023), e202302795.
- [46] H.B. Tao, L. Fang, J. Chen, H.B. Yang, J. Gao, J. Miao, S. Chen, B. Liu, Identification of surface reactivity descriptor for transition metal oxides in oxygen evolution reaction, *J. Am. Chem. Soc.* 138 (2016) 9978–9985.
- [47] J. Li, J. Hu, M. Zhang, W. Gou, S. Zhang, Z. Chen, Y. Qu, Y. Ma, A fundamental viewpoint on the hydrogen spillover phenomenon of electrocatalytic hydrogen evolution, *Nat. Commun.* 12 (2021) 3502.